Enhanced High-Temperature Energy Storage Performances in Polymer Dielectrics by Synergistically Optimizing Band-gap and Polarization of Dipolar Glass

Minzheng Yang[1], Weibin Ren*[1], Zenghui Jin[1], Erxiang Xu[1], Yang Shen*[1]

1. State Key Lab of New Ceramics and Fine Processing, Tsinghua University, School of Materials Science and Engineering, Beijing, China.

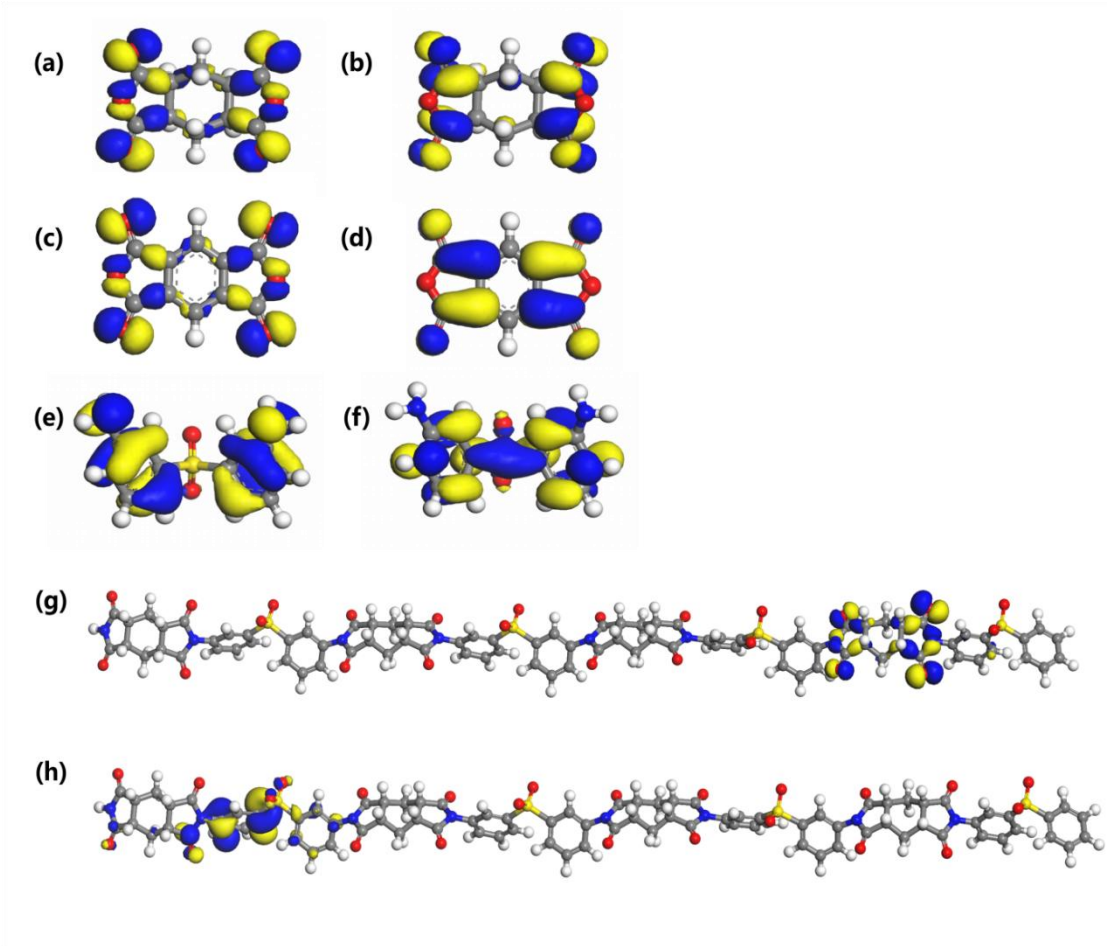

Figure S1. Energy level distribution of (a) HOMO and (b) LUMO of HPMDA, (c) HOMO and (d) LUMO of PMDA, (e) HOMO and (f) LUMO of NS, (g) HOMO and (h) LUMO of DG. Note that the localization of HOMO and LUMO in DG chain is induced by the structure optimization for a most stable state of the polymer chain. In the ideal polymer chain containing infinite monomers with same conformation and orientation, same positions in each monomer should have identical energy.

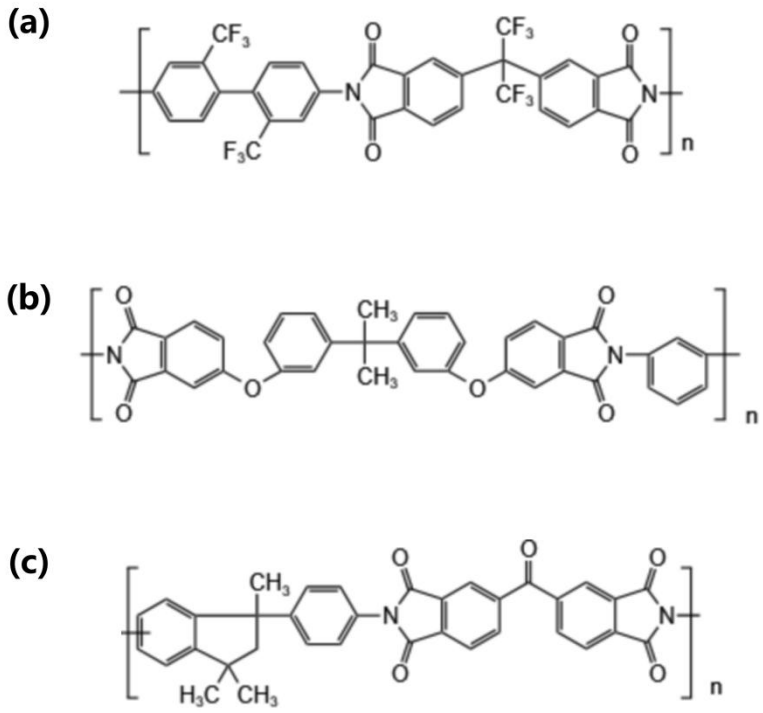

Figure S2. Chemical structures of PIs: (a) FPI, (b) PEI, and (c) SPI.

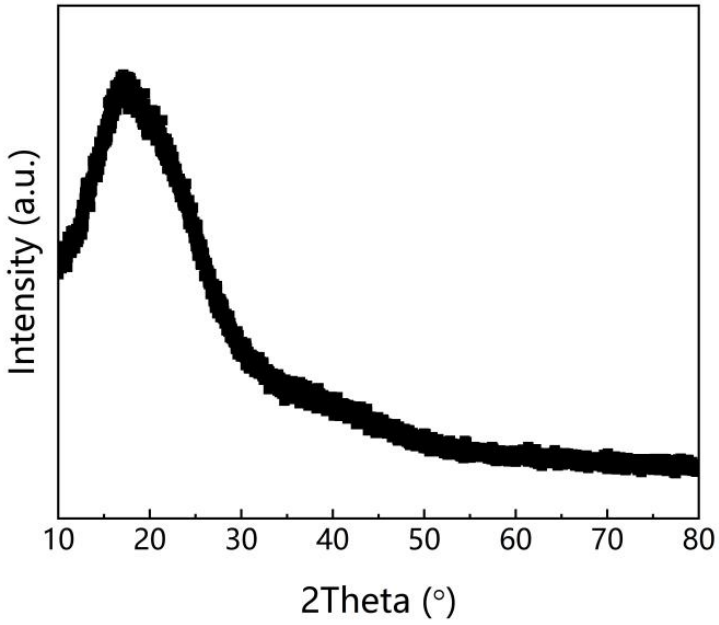

Figure S3. XRD curve of DG.

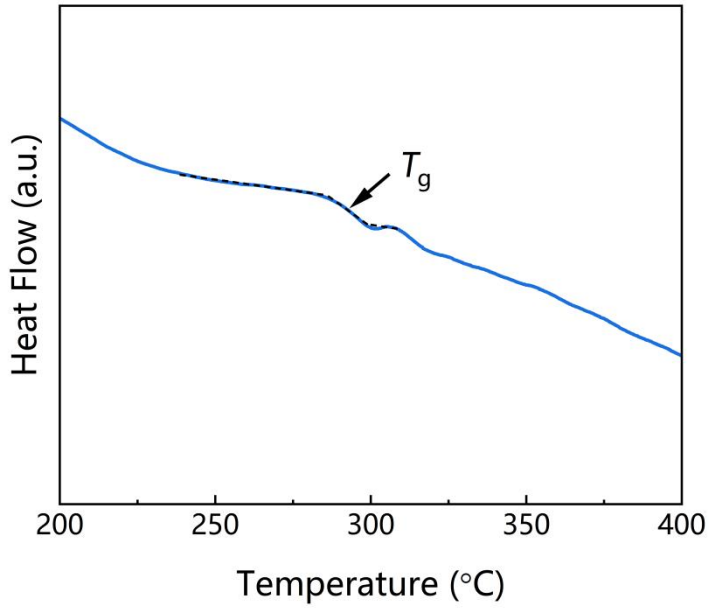

Figure S4. DSC curve of DG.

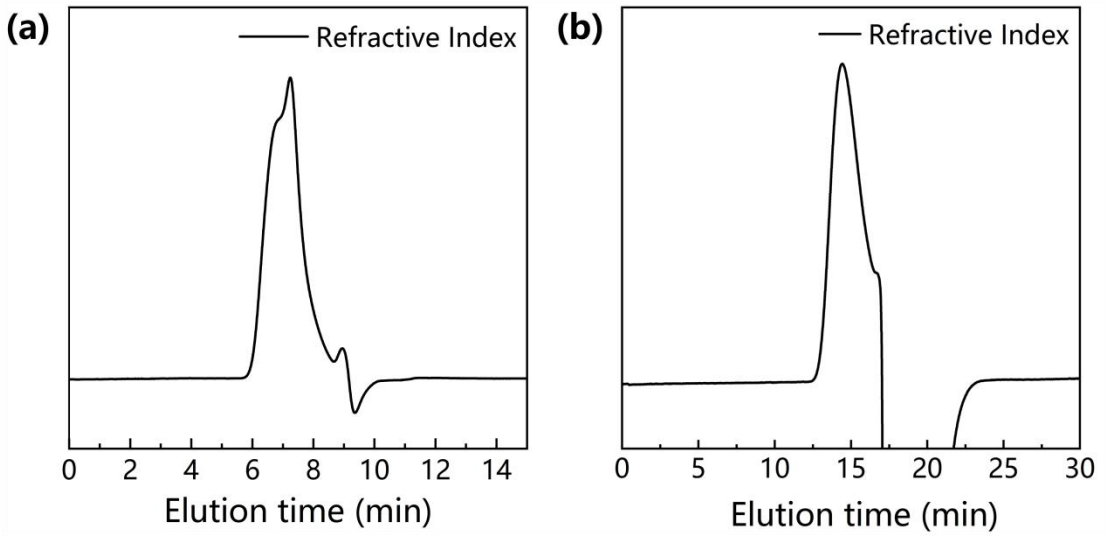

Figure S5. GPC traces of (a) FPI and (b) DG.

Table S1. Number-average molecular weight (M_n), weight-average molecular weight (M_w), polydispersity, and degree of polymerization (n) of FPI and DG.

	FPI	**DG**
M_n (g mol^{-1})	87496	38577
M_w (g mol^{-1})	276184	77578
Polydispersity	3.157	2.011
n	120	88

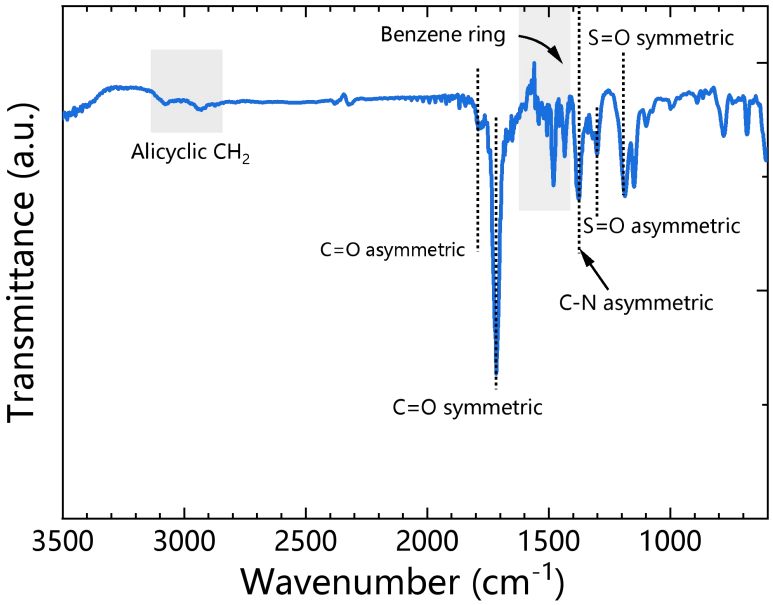

Figure S6. FTIR curve of DG.

Table S2. Characteristic absorption bands of DG.

Wave Number (cm^{-1})	
1193.29	S=O symmetric
1301.44	S=O asymmetric
1375.15	C-N asymmetric
1716.50	C=O symmetric
1791.42	C=O asymmetric

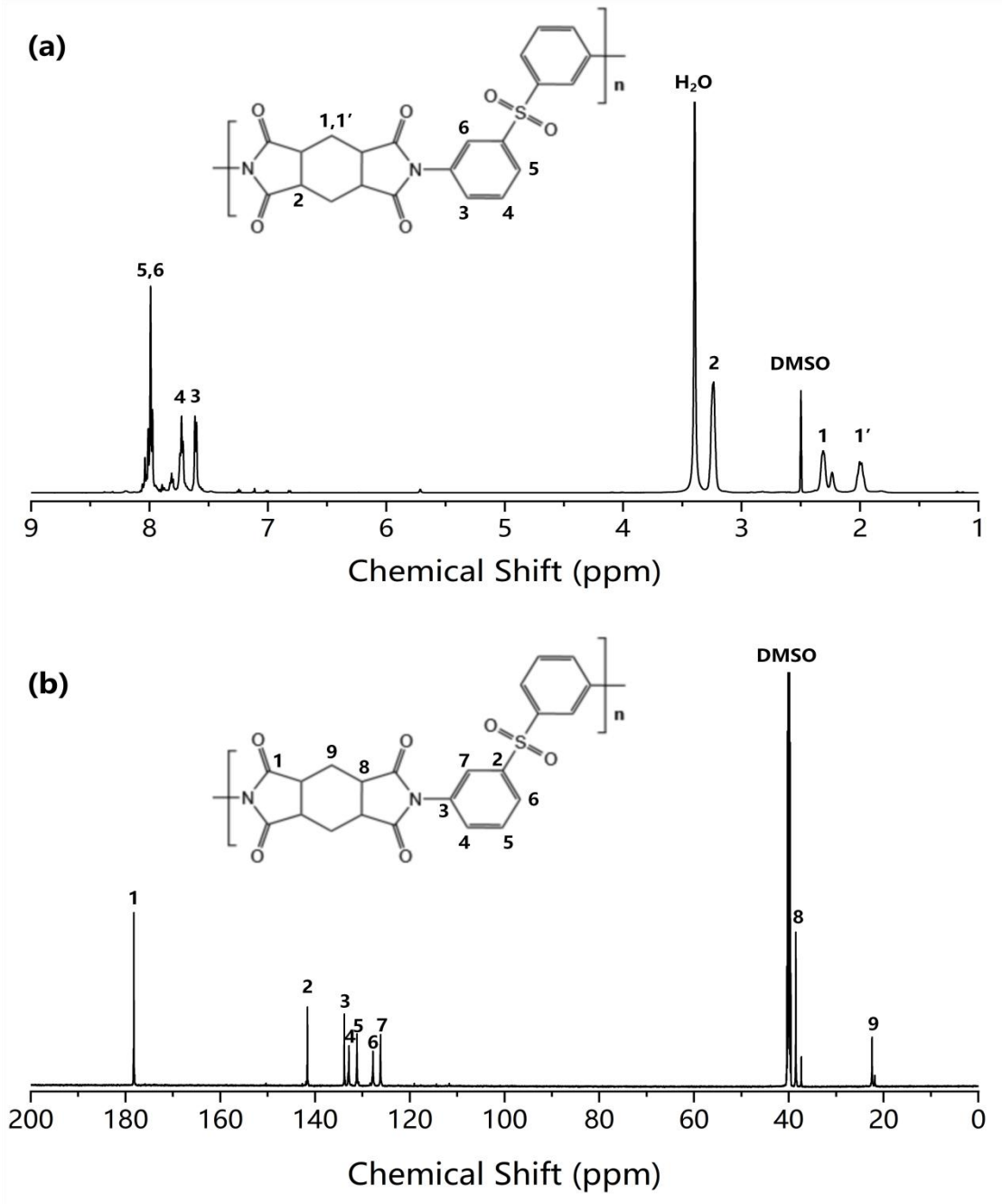

Figure S7. (a) ^{1}H and (b) ^{13}C NMR spectrum of DG.

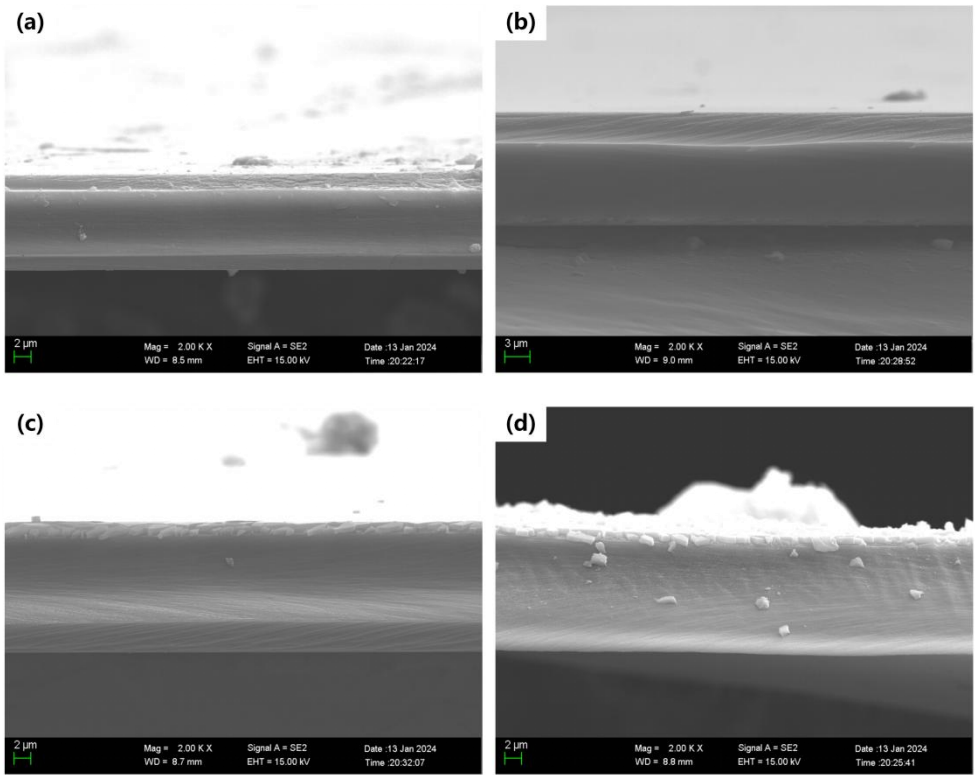

Figure S8. SEM images of cross-sections of (a) FPI, (b) FPI-8 wt% DG, (c) FPI-8 wt% HPMDA, and (d) FPI-8 wt% NS.

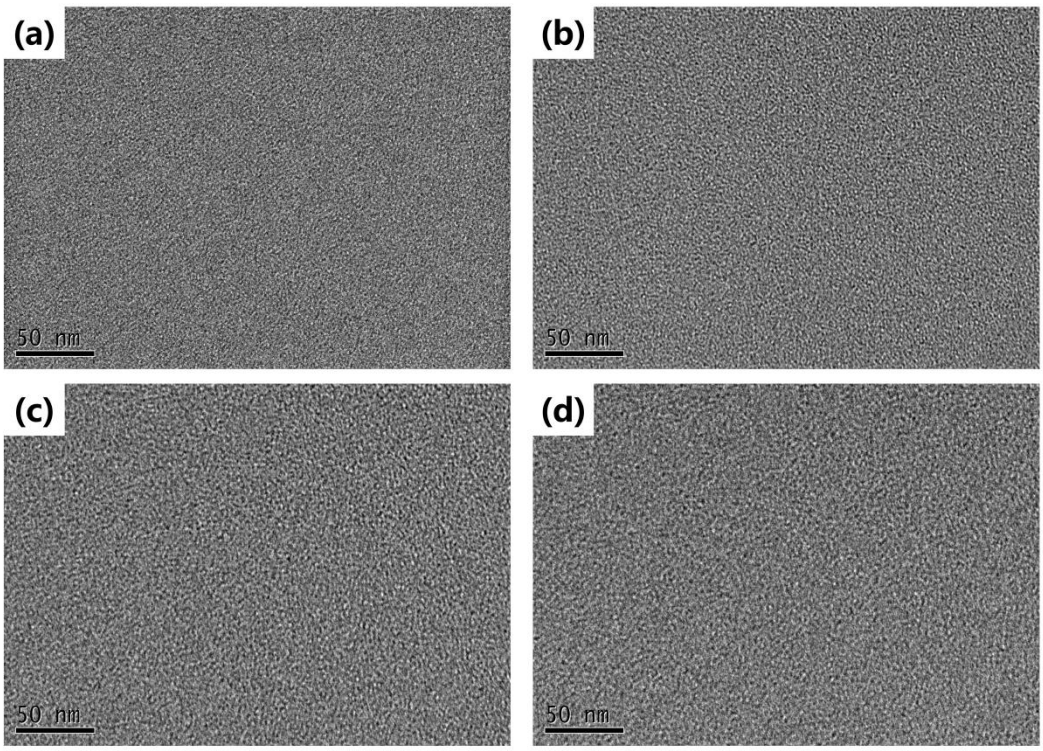

Figure S9. TEM images of cross-sections of (a) FPI, (b) FPI-8 wt% DG, (c) FPI-8 wt% HPMDA, and (d) FPI-8 wt% NS.

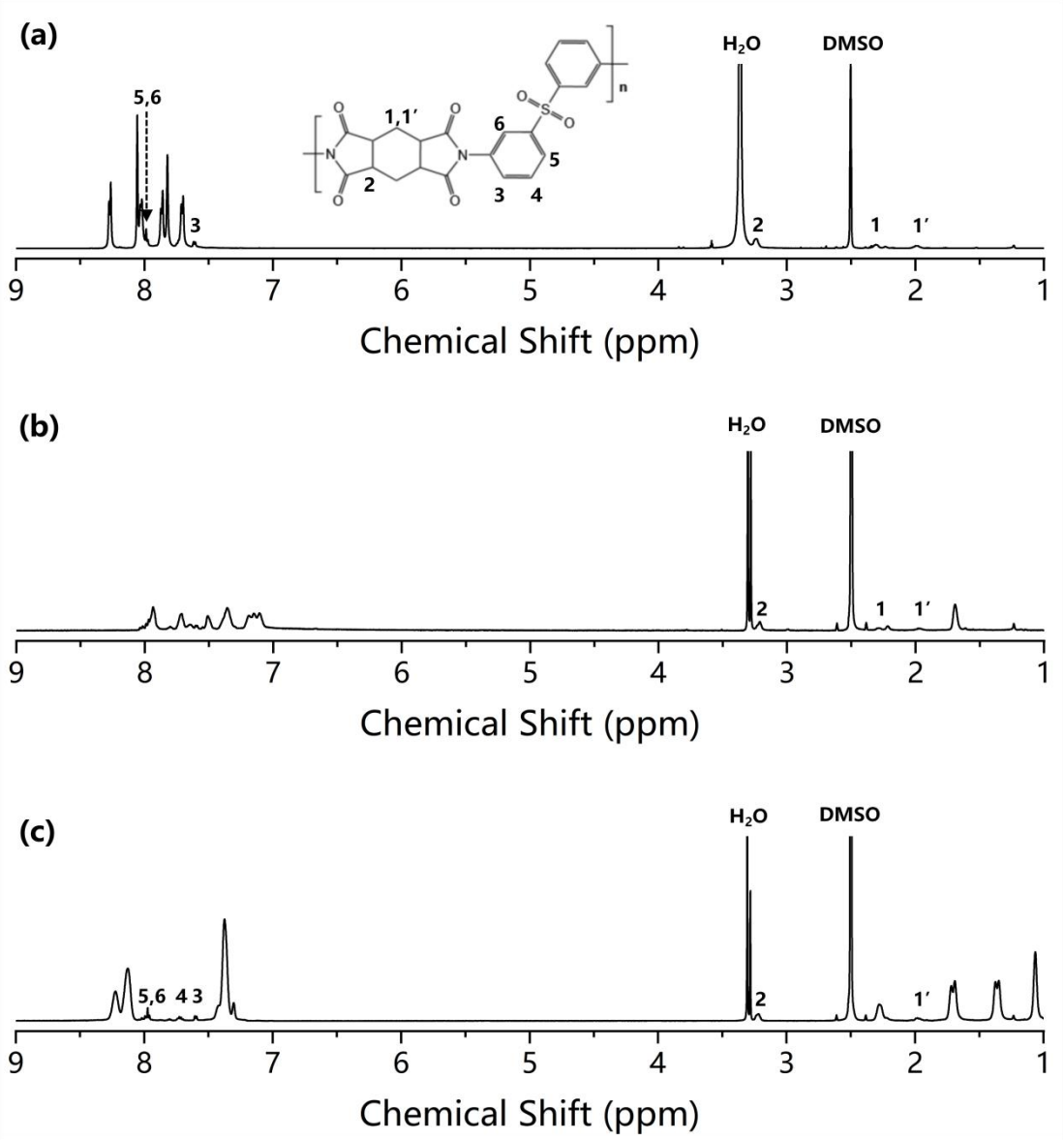

Figure S10. ^{1}H NMR spectrum of (a) FPI-8 wt% DG, (b) PEI-8 wt% DG (c) SPI-8 wt% DG. The characteristic peaks of DG that do not overlap with the peaks of other polymers are marked. The preparation of FPI-DG involves DMF, and the preparation of PEI-DG and SPI-DG involves NMP. The characteristic peaks of DMF include 2.9 (the strongest) and 8.0 ppm. The characteristic peaks of NMP include 2.03, 2.37, 2.85 (the strongest), and 3.39 ppm. As seen, there is no obvious peak at these positions. The two small peaks symmetrical along the DMSO peaks in (b) and (c) are the satellite peaks, which is induced by the couplings of ^{13}C to H atoms.

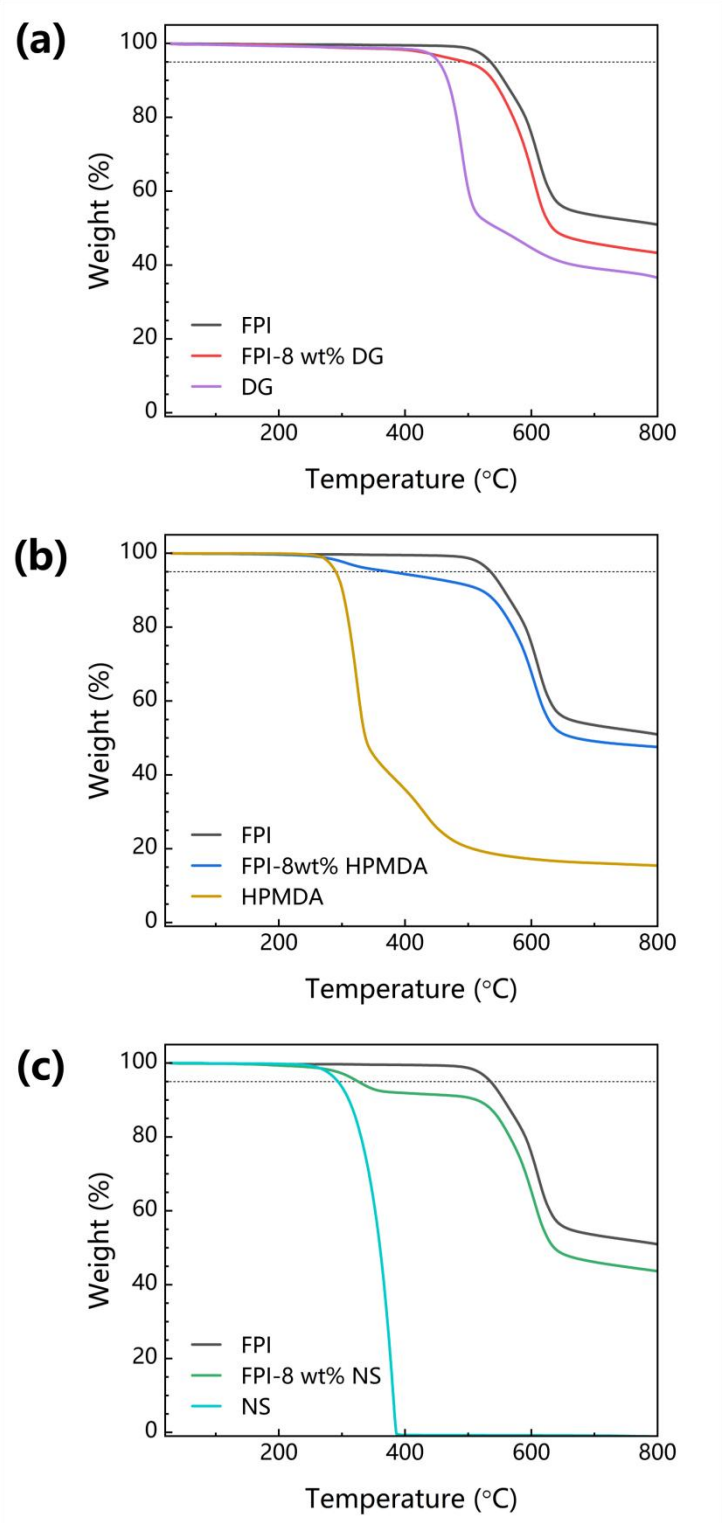

Figure S11. TGA curves of FPI and (a) FPI-8 wt% DG and DG, (b) FPI-8 wt% HPMDA and HPMDA, and (c) FPI-8 wt% NS and NS.

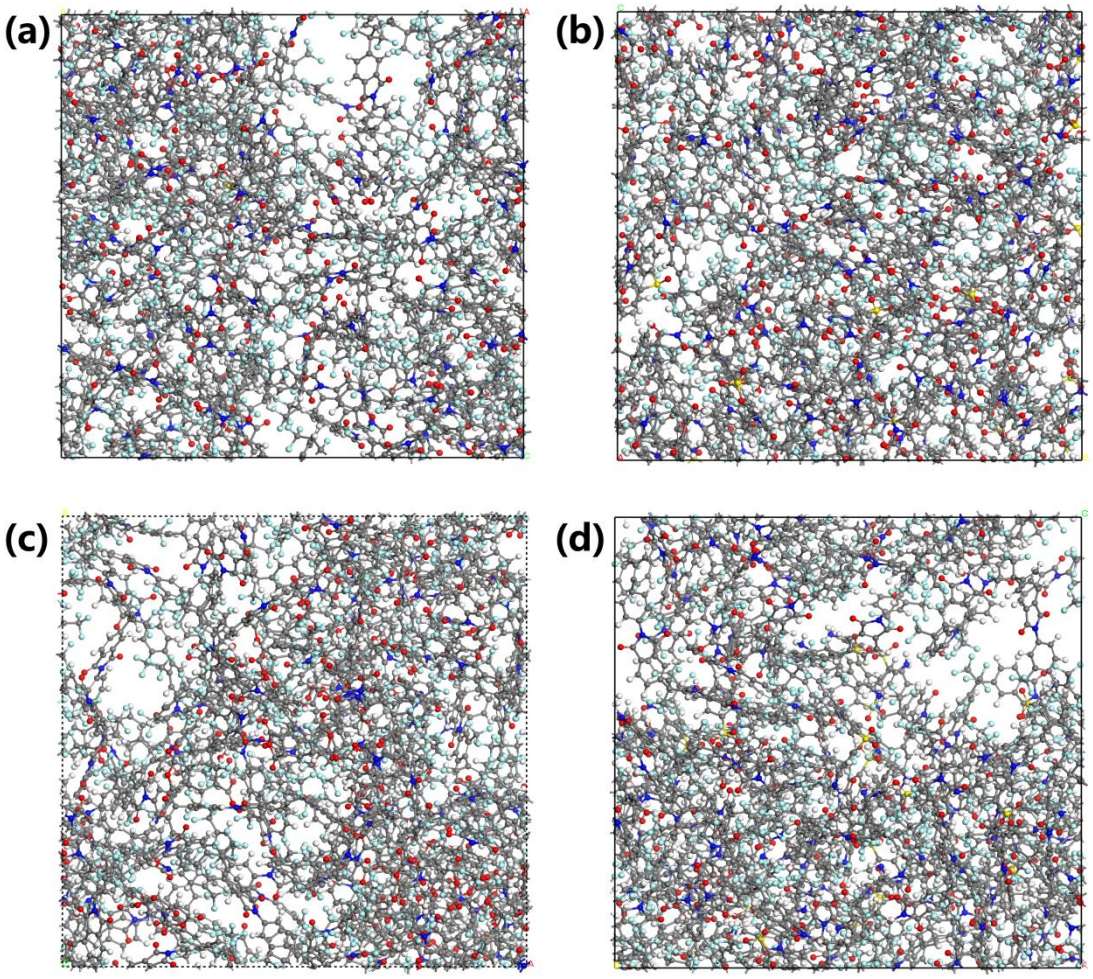

Figure S12. MD cells of (a) FPI, (b) FPI-8 wt% DG, (c) FPI-8 wt% HPMDA, and (d) FPI-8 wt% NS.

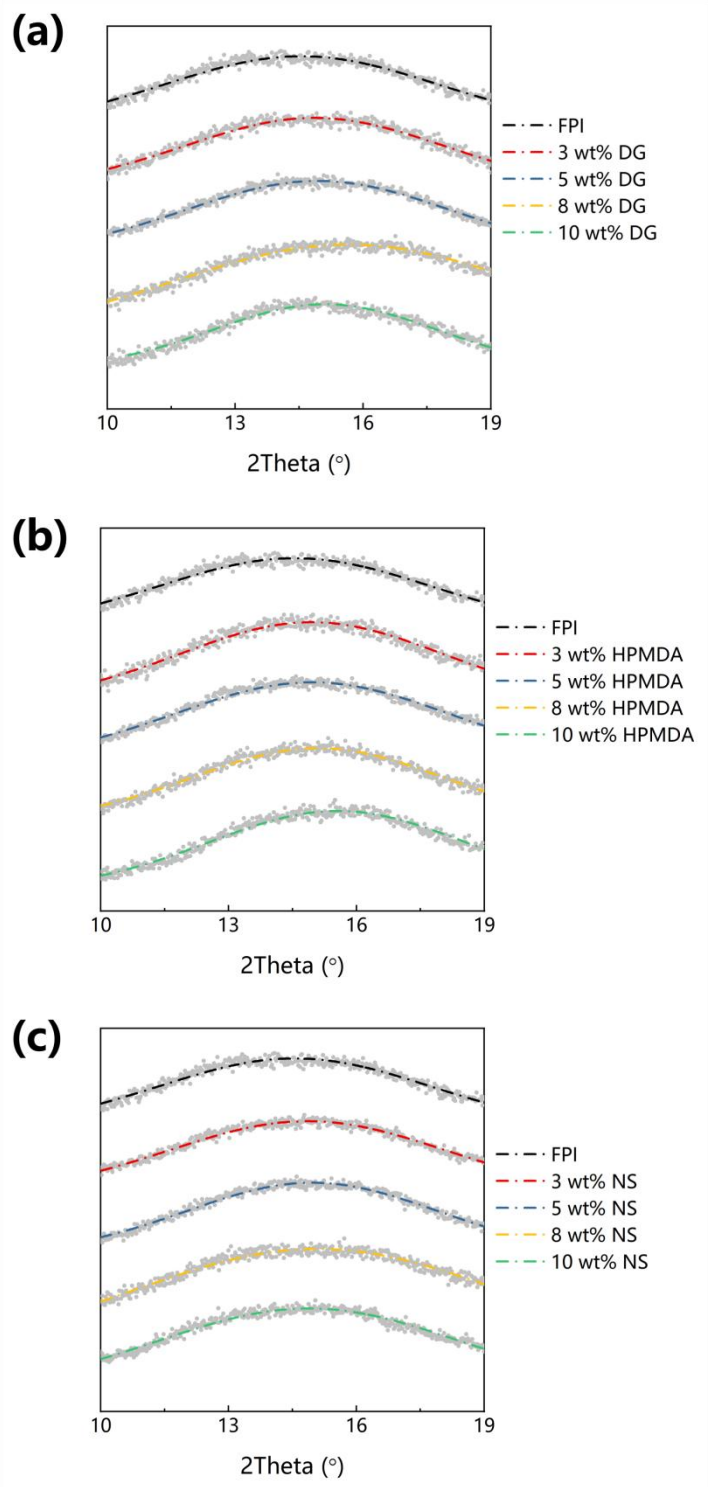

Figure S13. XRD curves of (a) FPI-DG, (b) FPI-HPMDA, and (c) FPI-NS.

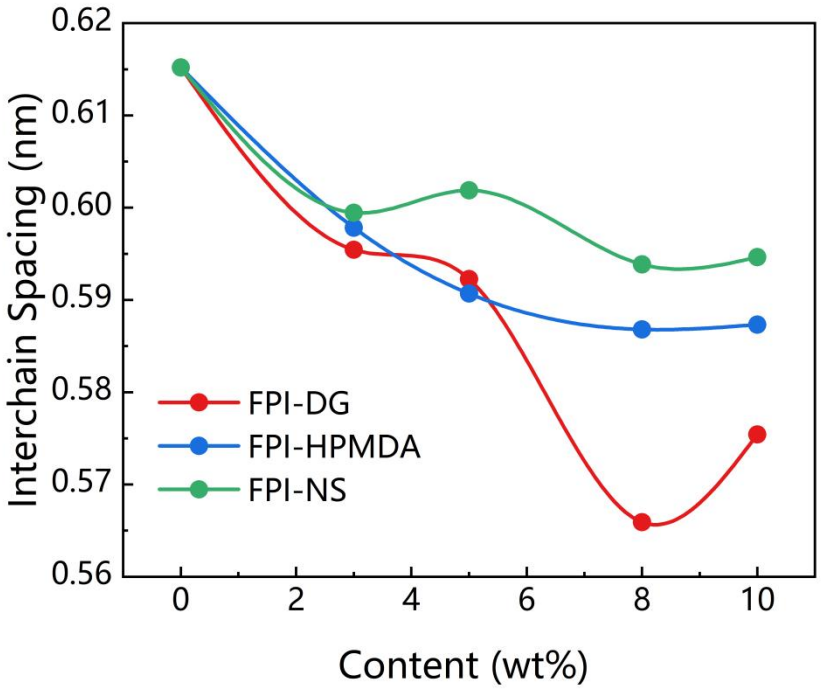

Figure S14. Interchain spacing values of FPI-DG, FPI-HPMDA, and FPI-NS. Considering that the data points were fitted from the XRD curves and the differences between some data points are too small (< 0.01 nm), the size relationships between a few data points may not be very accurate. However, FPI-DG obviously exhibits lower interchain spacing than FPI-HPMDA and FPI-NS, which is the most important and desired result of XRD characterization in this study.

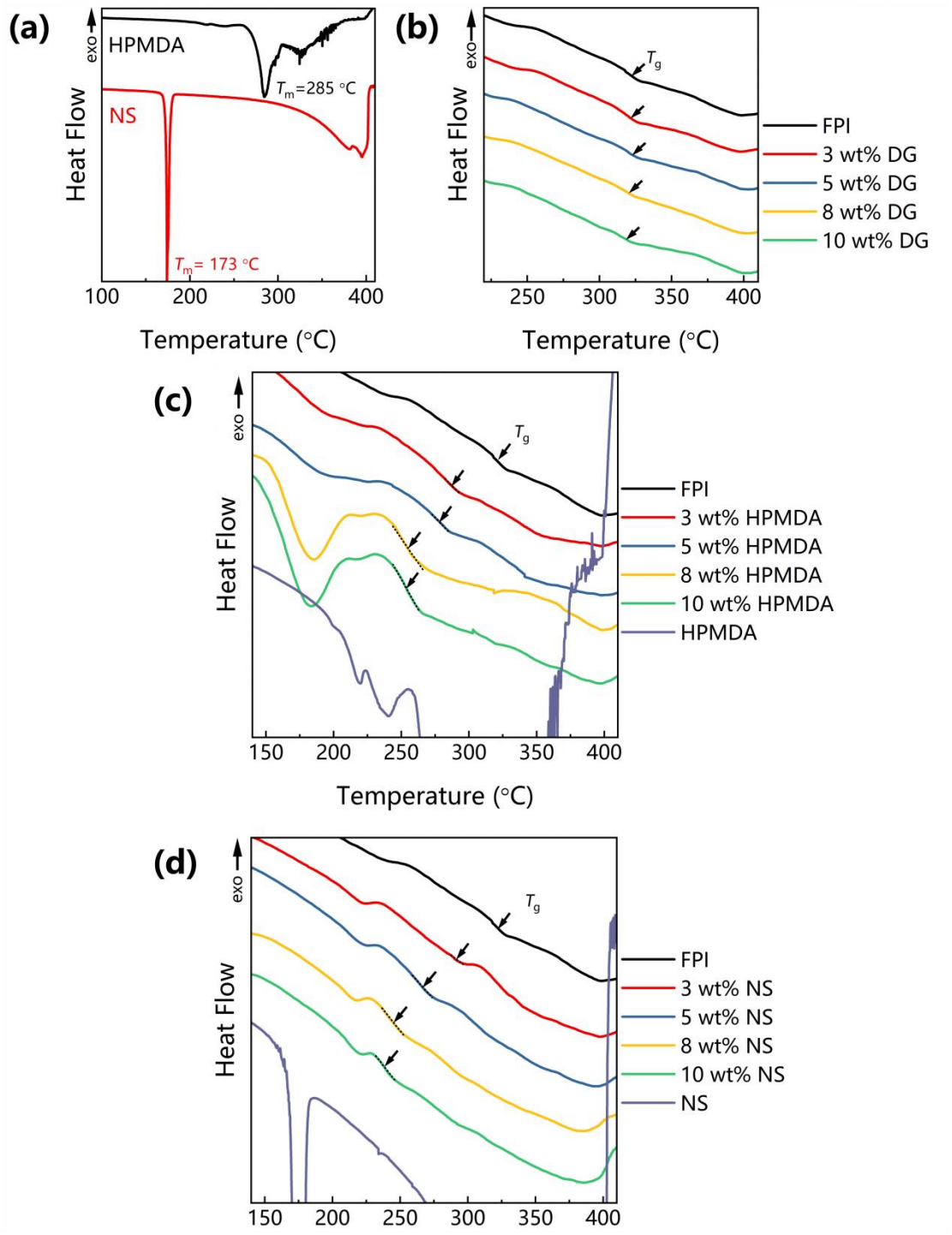

Figure S15. DSC curves of (a) pure HPMDA and NS, (b) FPI-DG, (c) FPI-HPMDA, and (d) FPI-NS.

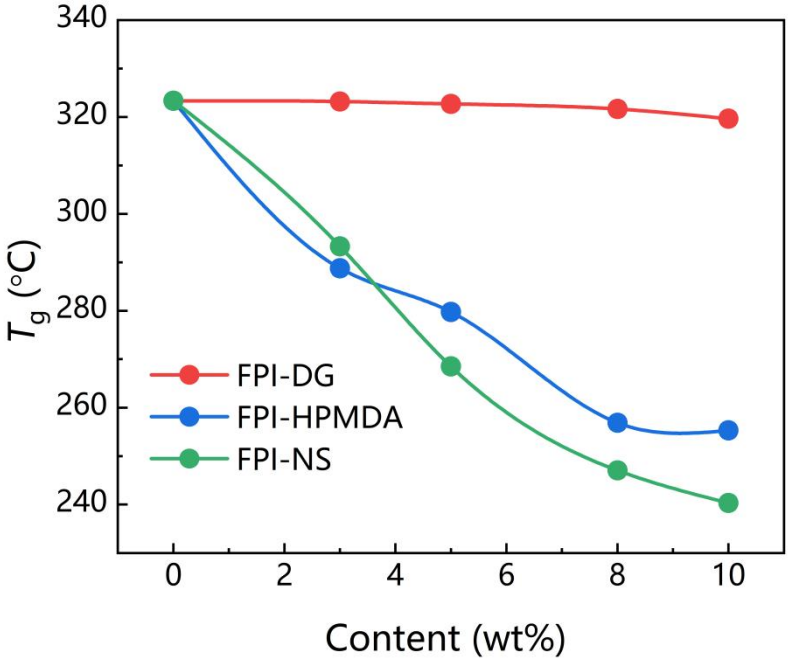

Figure S16. T_g values of FPI-DG, FPI-HPMDA, and FPI-NS.

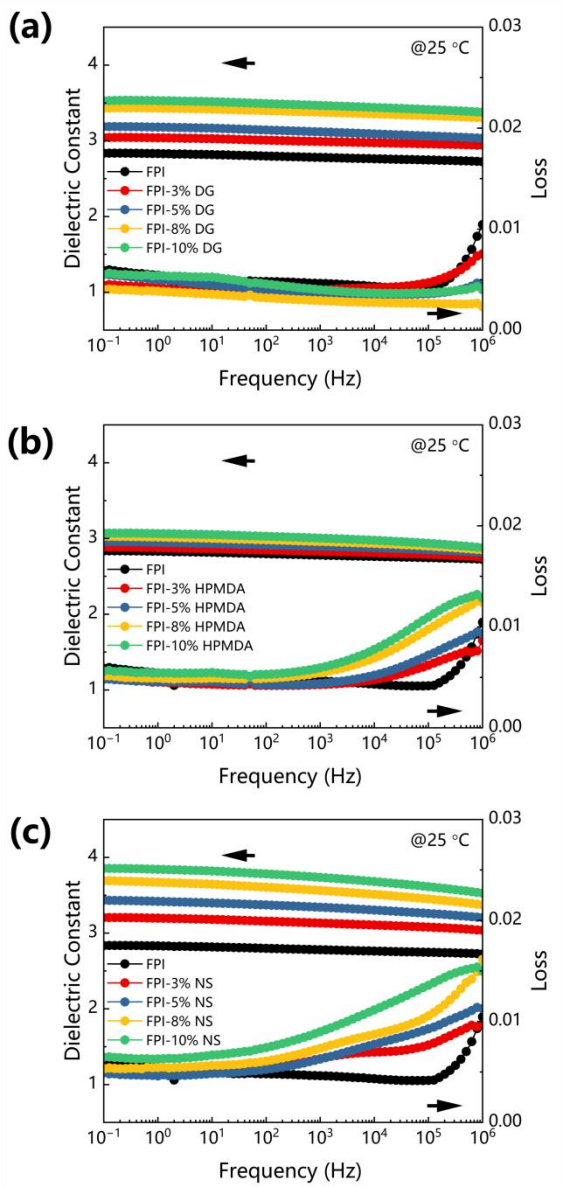

Figure S17. Dielectric spectra versus frequency of (a) FPI-DG, (b) FPI-HPMDA, and (c) FPI-NS at 25 ℃.

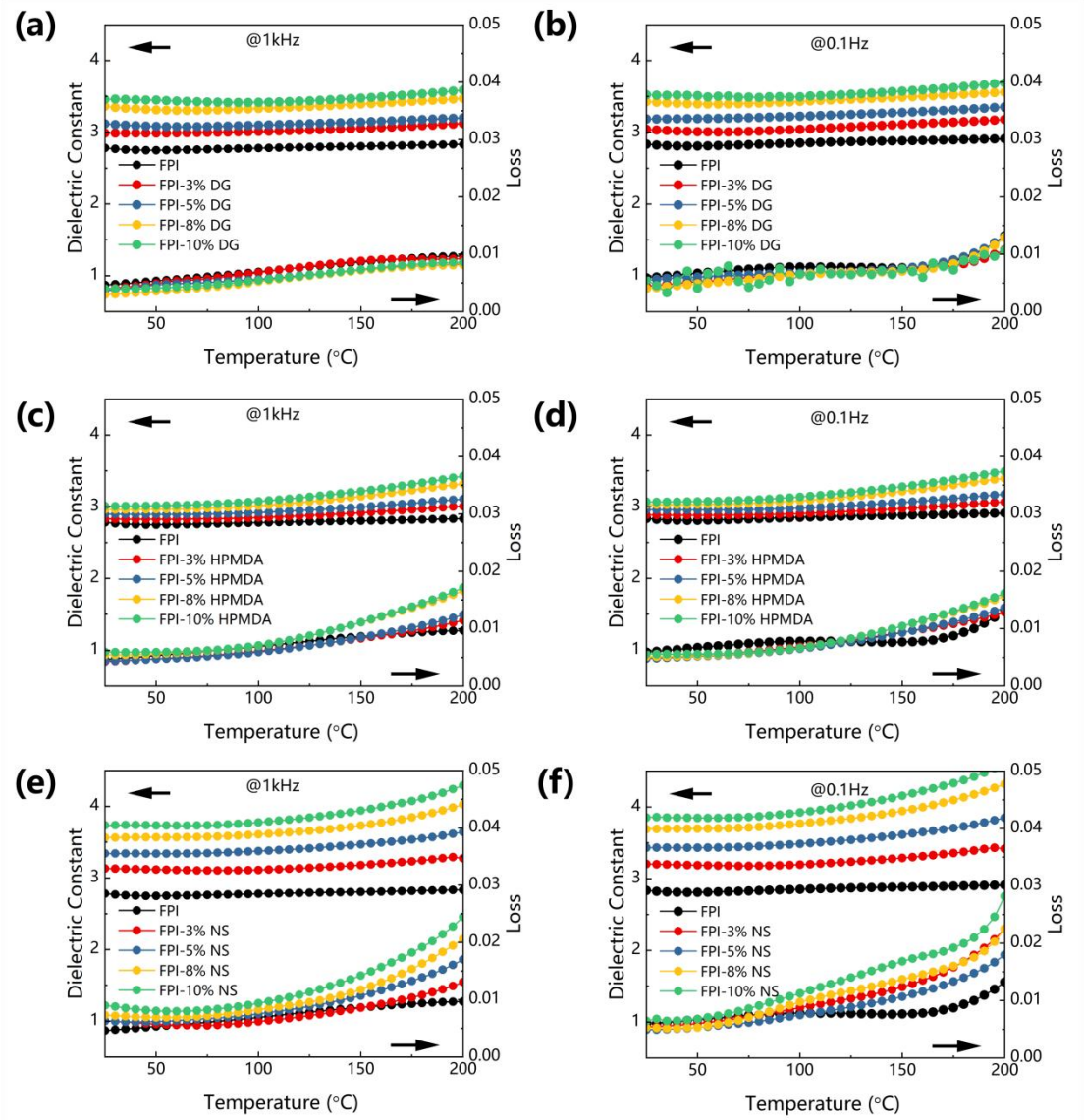

Figure S18. Dielectric spectra versus temperature of (a, b) FPI-DG, (c, d) FPI-HPMDA, and (e, f) FPI-NS at 1000 Hz and 0.1 Hz.

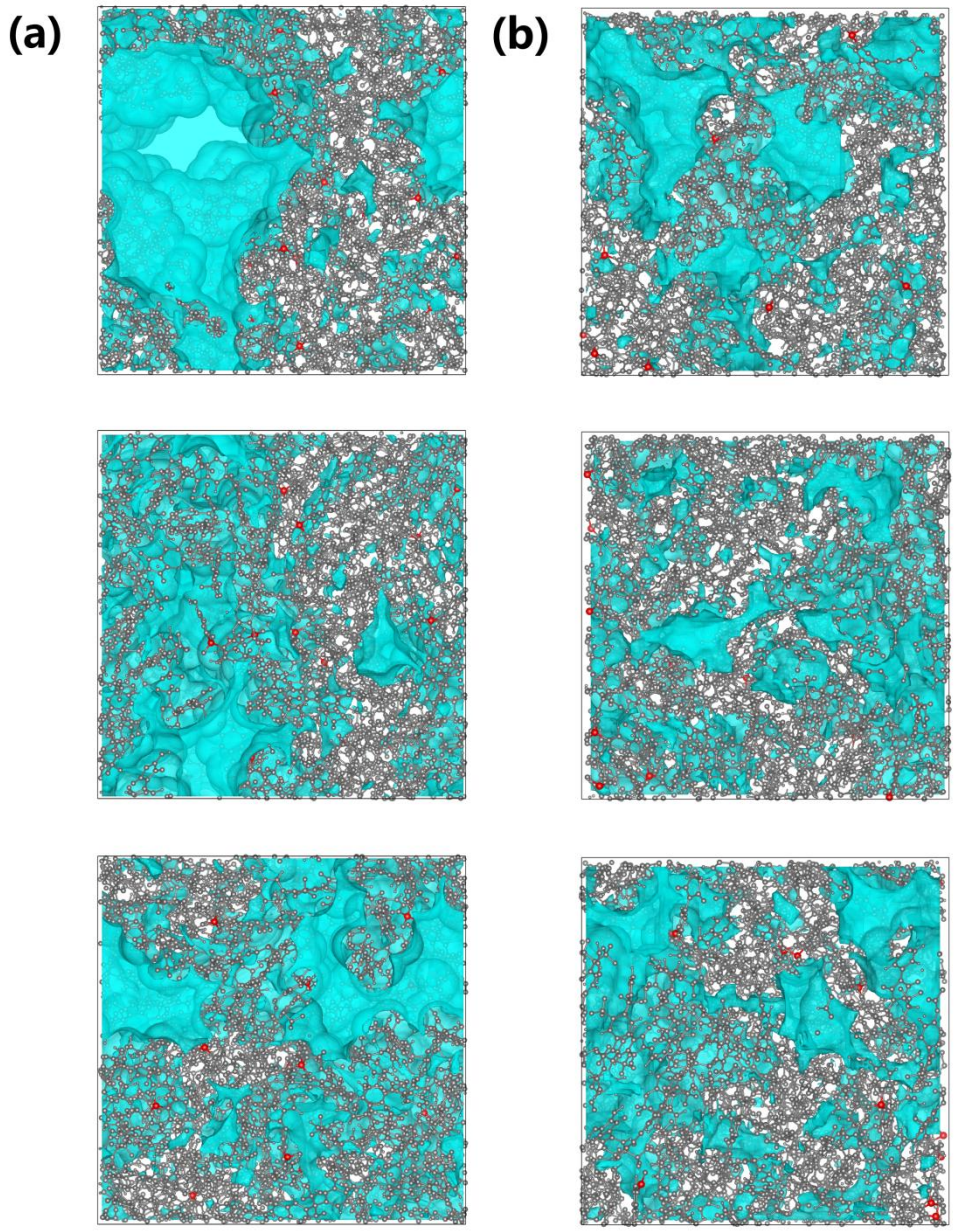

Figure S19. Distribution of free volume (blue) and S atoms (red) in (a) FPI-8 wt% NS and (b) FPI-8 wt% DG cells.

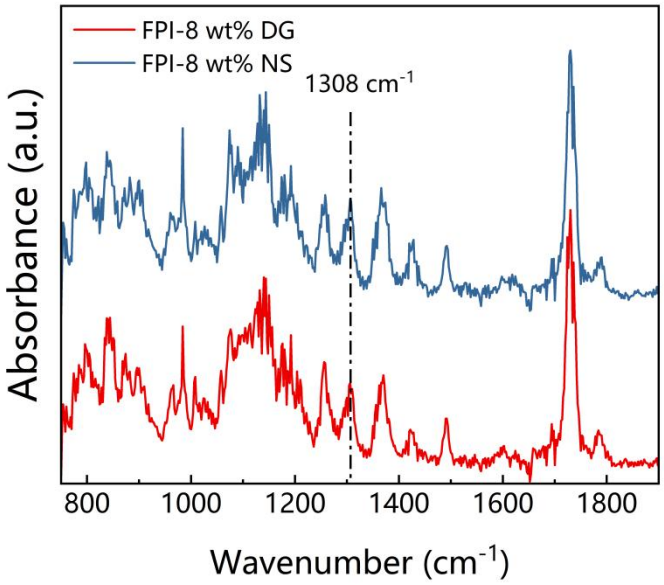

Figure S20. IR spectra of FPI-8 wt% DG and FPI-8 wt% NS obtained by AFM-IR. The peak at 1308 cm^{-1} can be attributed to the S=O asymmetric stretching mode.

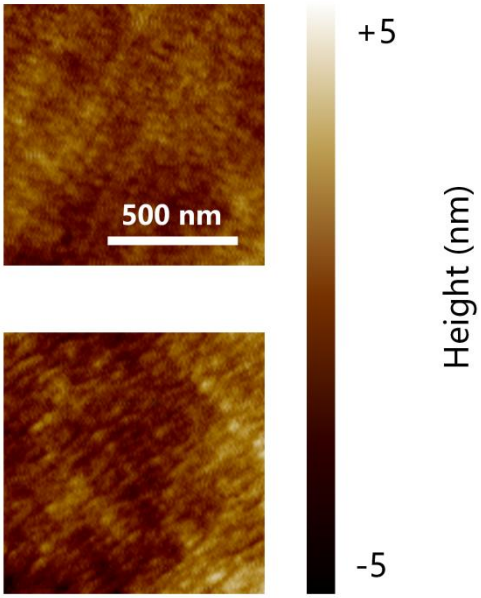

Figure S21. AFM-IR topography images of FPI-8 wt% NS (upper) and FPI-8 wt% DG (lower).

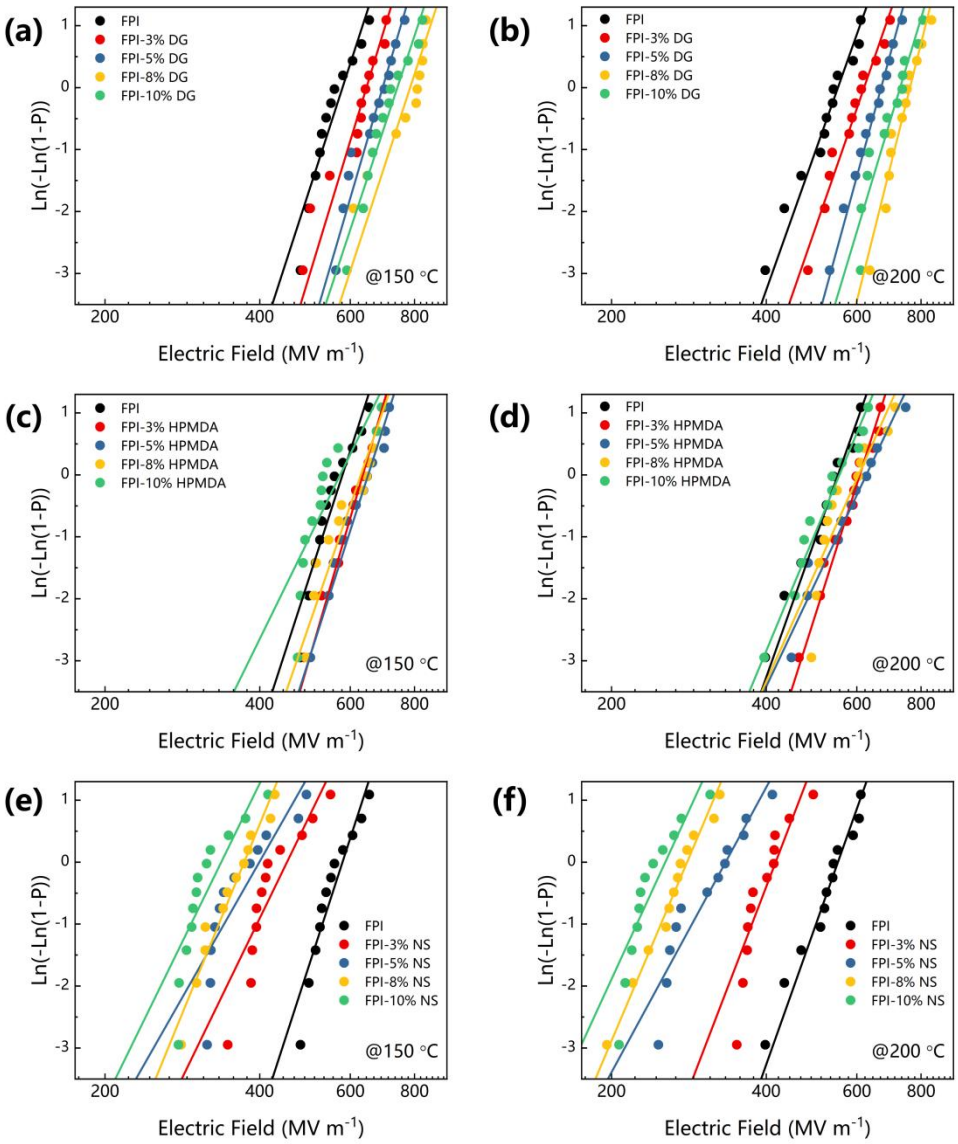

Figure S22. Breakdown electric field Weibull distribution at high temperatures of (a, b) FPI-DG, (c, d) FPI-HPMDA, and (e, f) FPI-NS.

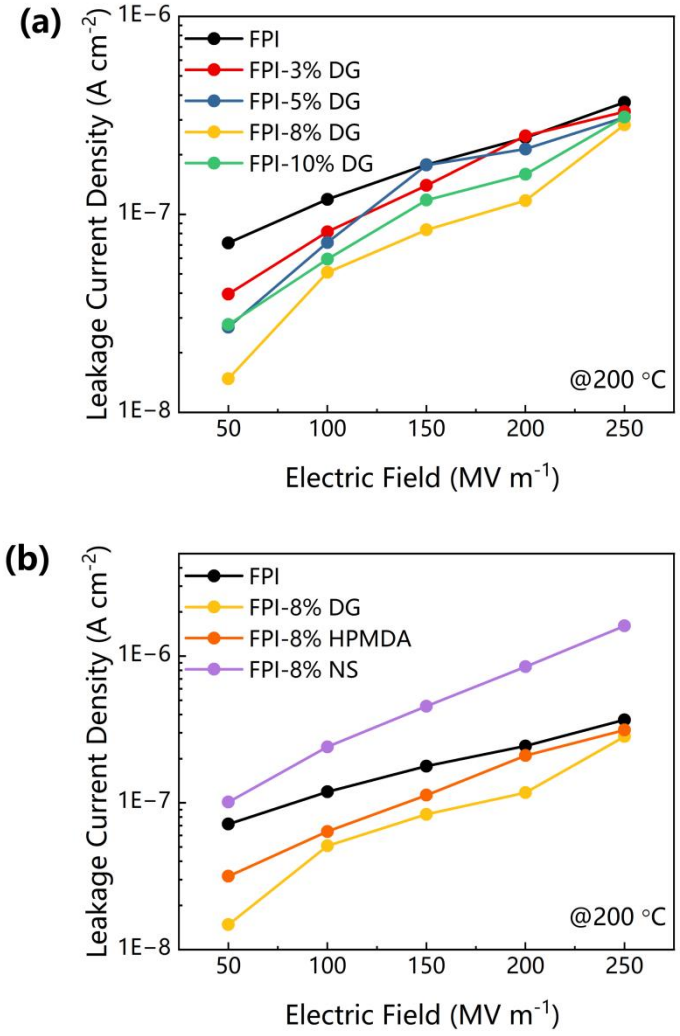

Figure S23. Leakage current density versus electric field at 200 °C of (a) FPI-DG blends and (b) FPI-based dielectrics with the introduction content of 8 wt%.

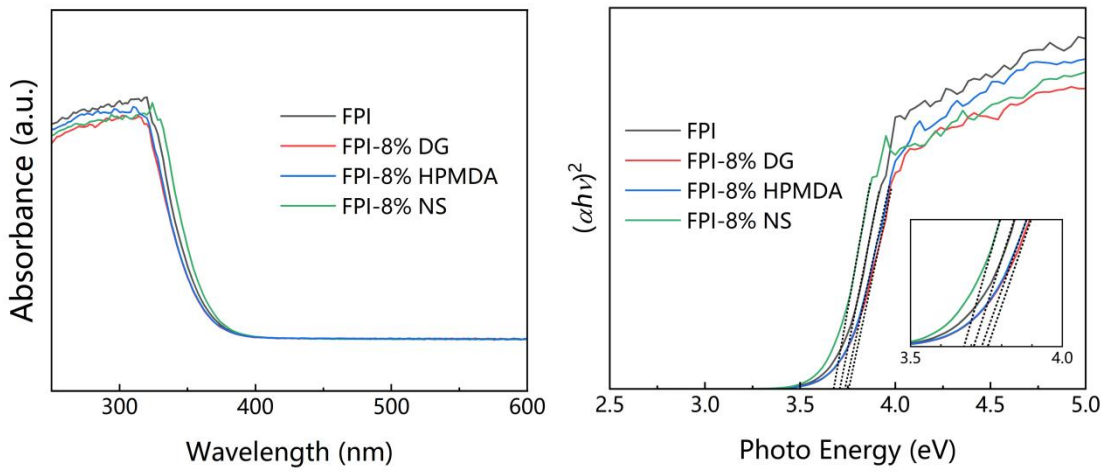

Figure S24. UV-Vis spectra of FPI-8 wt% DG, FPI-8 wt% HPMDA, and FPI-8 wt% NS.

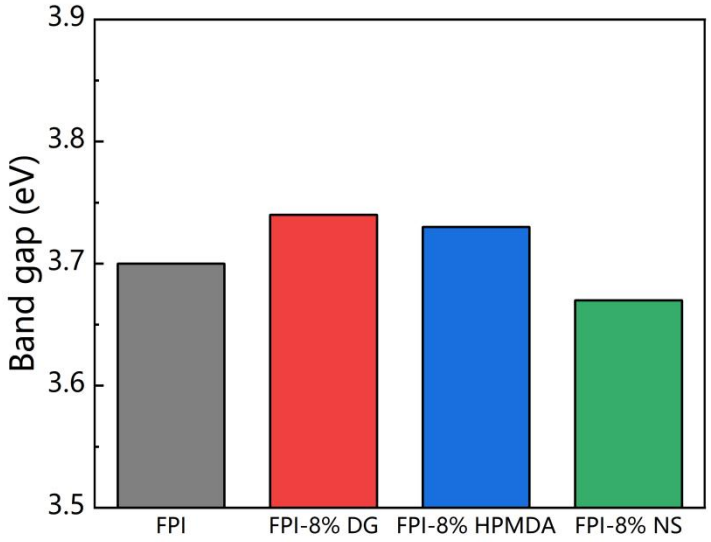

Figure S25. Optical E_g of FPI, FPI-8 wt% DG, FPI-8 wt% HPMDA, and FPI-8 wt% NS.

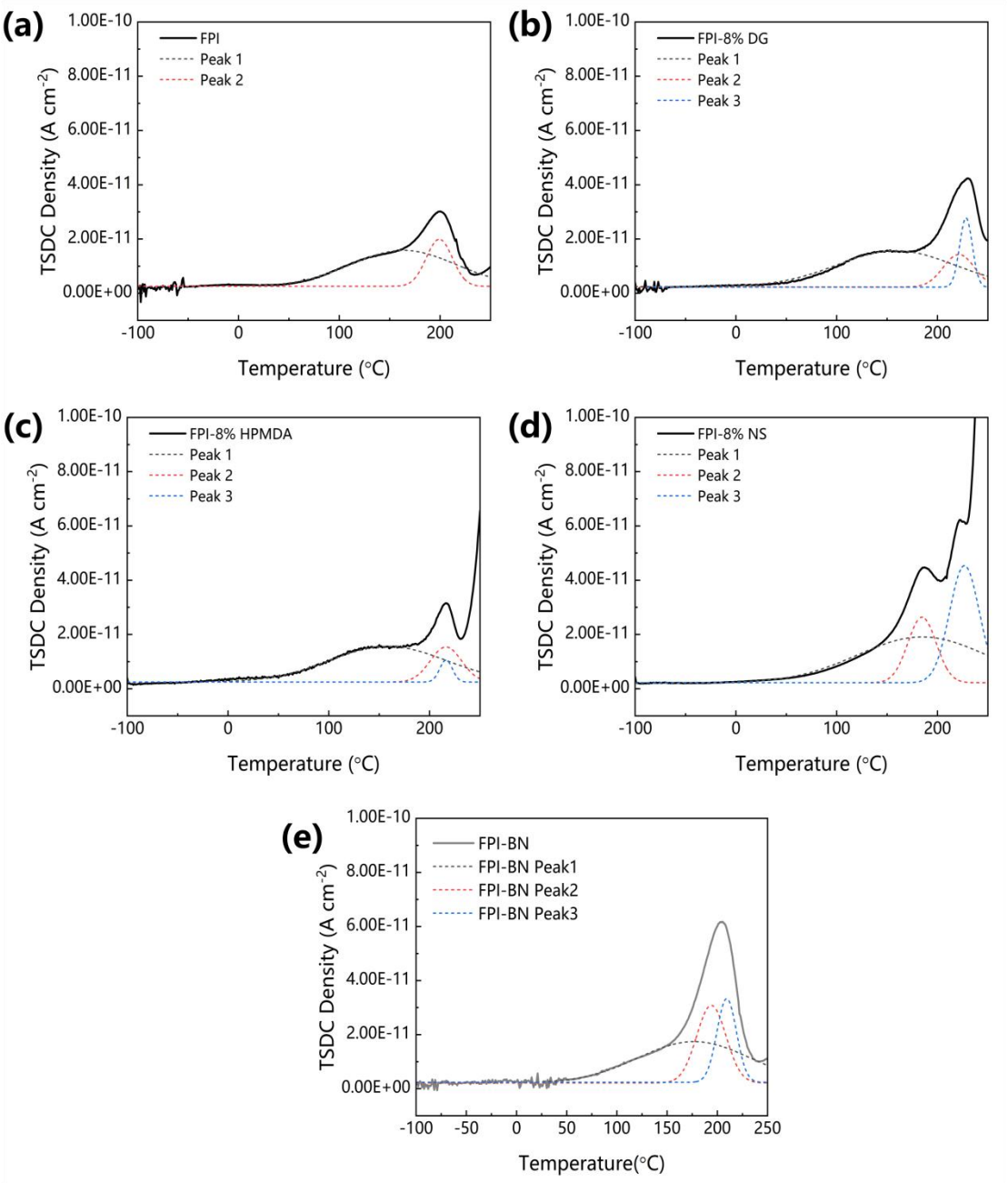

Figure S26. TSDC curves of (a) FPI, (b) FPI-8 wt% DG, (c) FPI-8 wt% HPMDA, and (d) FPI-8 wt% NS, (e) FPI-3 wt% BN.

Table S3. Trap depth and trap density of FPI and FPI-based dielectrics.

	Trap depth of Peak 2 (°C)	**Trap Density of Peak 2 (10^{20} m^{-3})**	**Trap depth of Peak 3 (°C)**
FPI	199.12	0.58	
FPI-8% DG	220.47	0.468	228.09
FPI-8% HPMDA	215.38	0.504	216.28
FPI-8% NS	184.38	0.958	226.50
FPI-3% BN	193.69	1.164	209.18

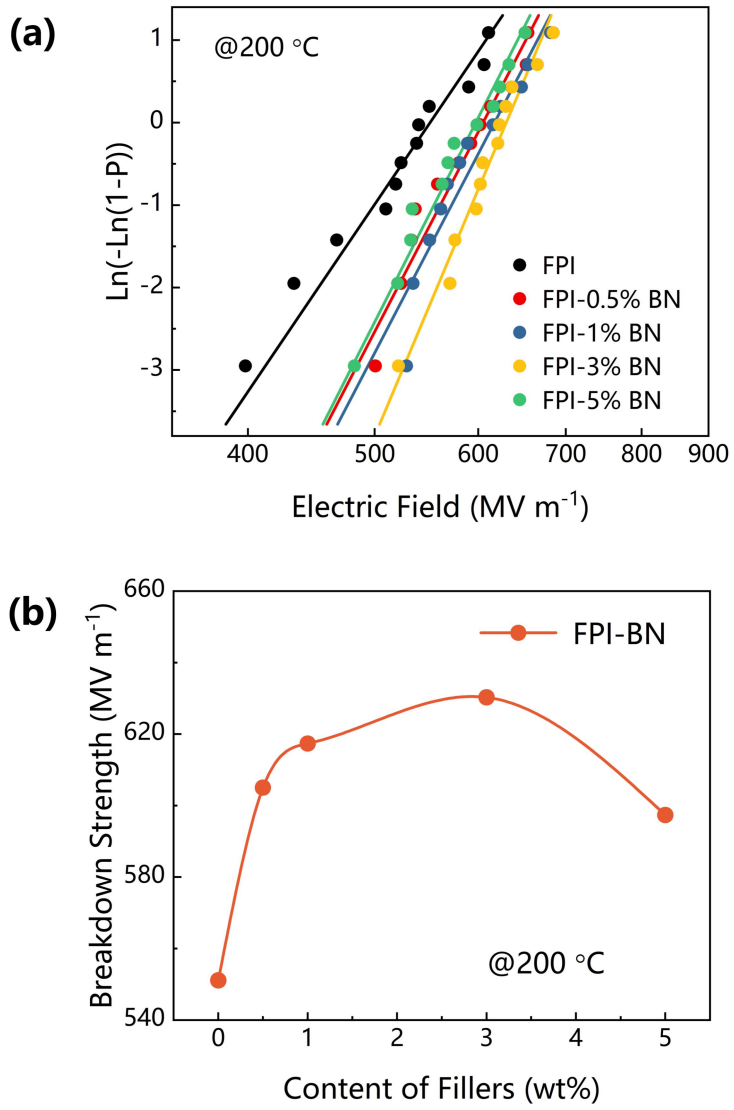

Figure S27. (a) Breakdown electric field Weibull distribution of FPI-BN composites with different filler content at 200 °C. (b) Breakdown strength of FPI-BN composites versus filler content at 200 °C.

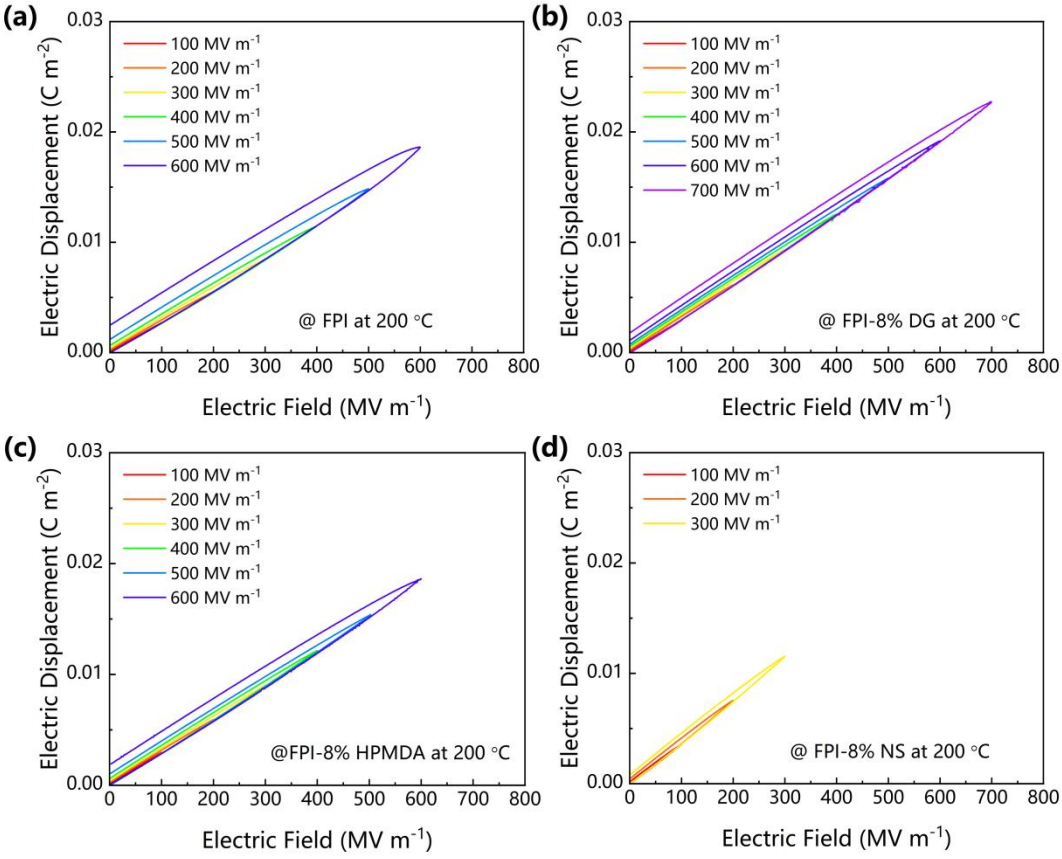

Figure S28. *D-E* loops at 200 °C of (a) FPI, (b) FPI-8 wt% DG, (c) FPI-8 wt% HPMDA, and (d) FPI-8 wt% NS.

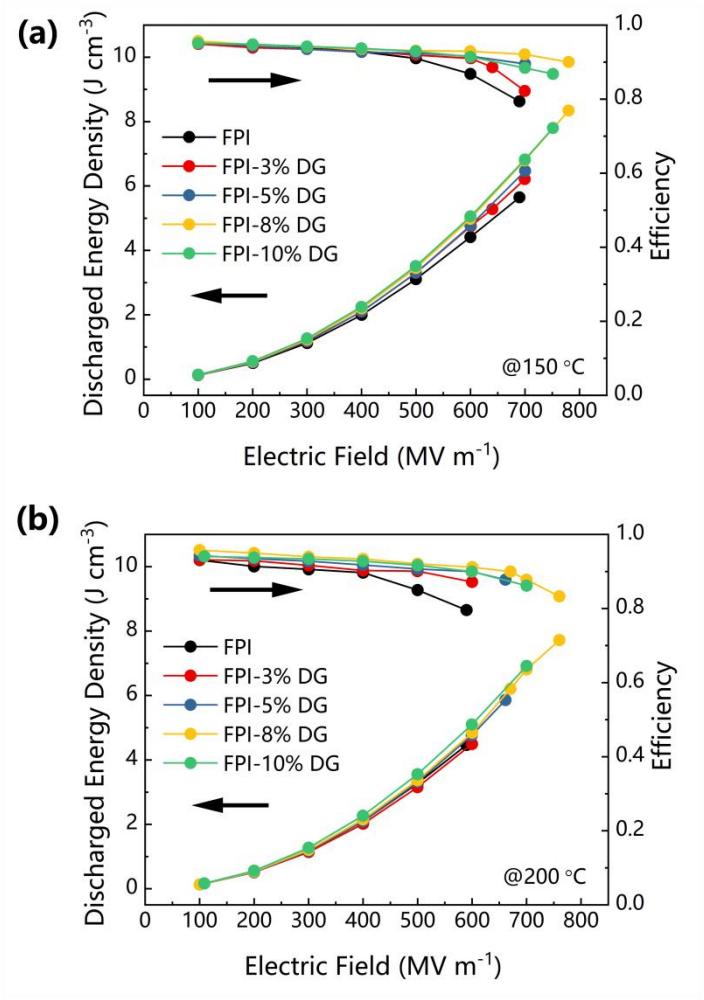

Figure S29. U_d and η versus electric field of FPI-DG blends at (a) 150 °C and (b) 200 °C.

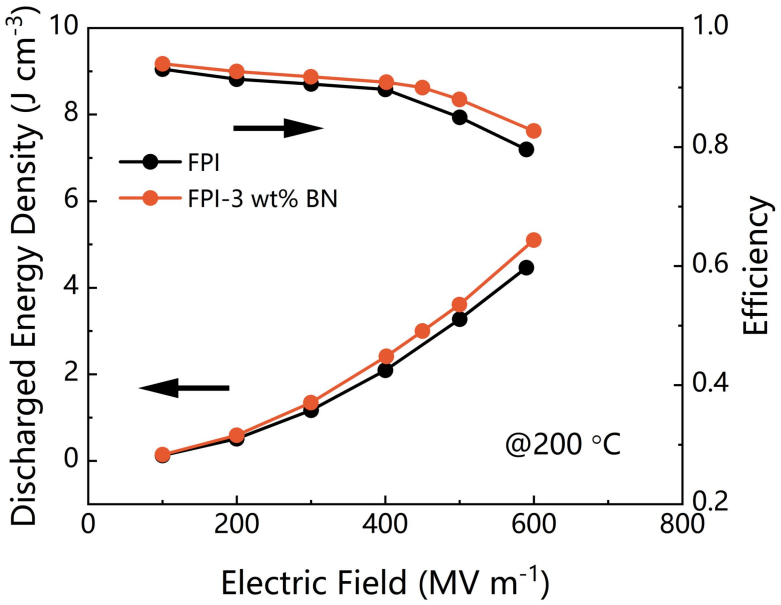

Figure S30. U_d and η versus electric field of FPI and FPI-3 wt% BN at 200 °C.

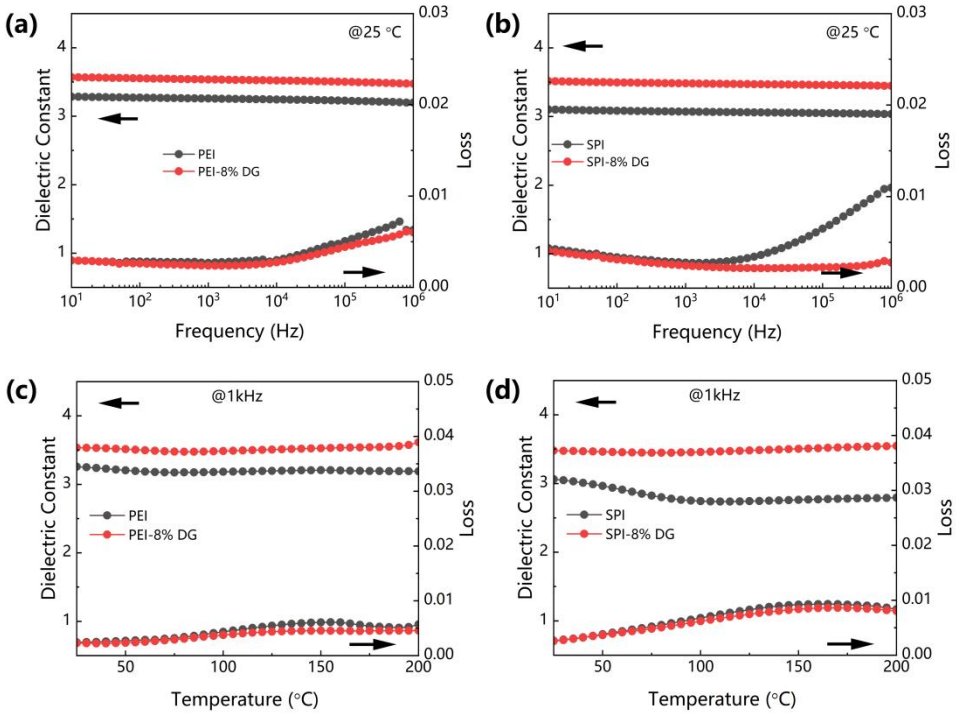

Figure S31. Dielectric spectra versus frequency and temperature of (a, c) PEI-8 wt% DG and (b, d) SPI-8 wt% DG.

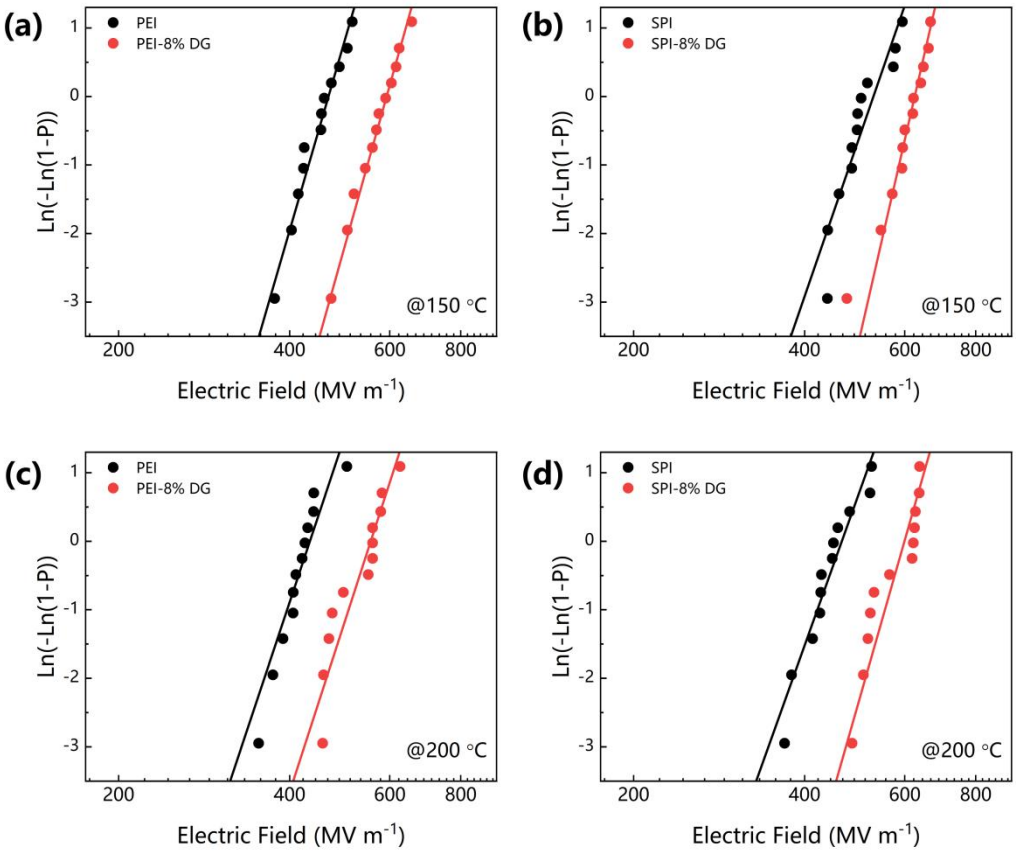

Figure S32. Breakdown electric field Weibull distribution at high temperatures of (a, c) PEI-8 wt% DG and (b, d) SPI-8 wt% DG.

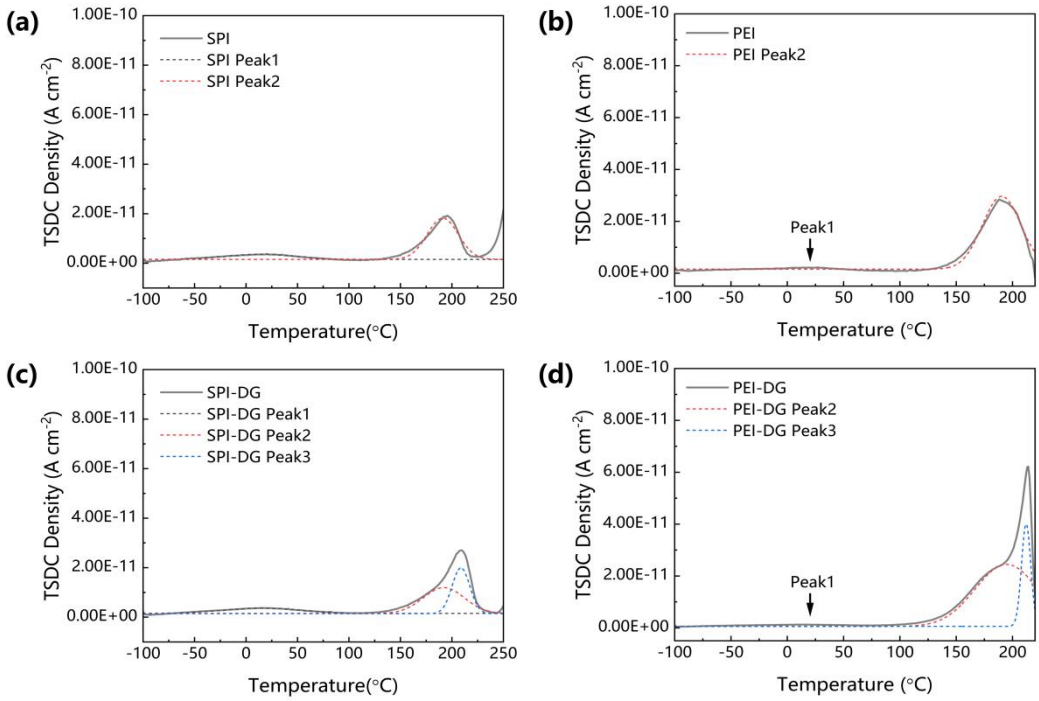

Figure S33. TSDC curves of (a) SPI, (b) PEI, (c) SPI-8 wt% DG, and (d) PEI-8 wt% DG.

Table S4 Trap parameters of TSDC curves of SPI, PEI, and their blends.

	Trap depth of Peak 2 (°C)	**Trap Density of Peak 2 (10^{20} m^{-3})**	**Trap depth of Peak 3 (°C)**
SPI	191.12	0.607	-
SPI-8% DG	192.09	0.499	208.77
PEI	190.21	1.284	-
PEI-8% DG	194.65	1.238	212.04

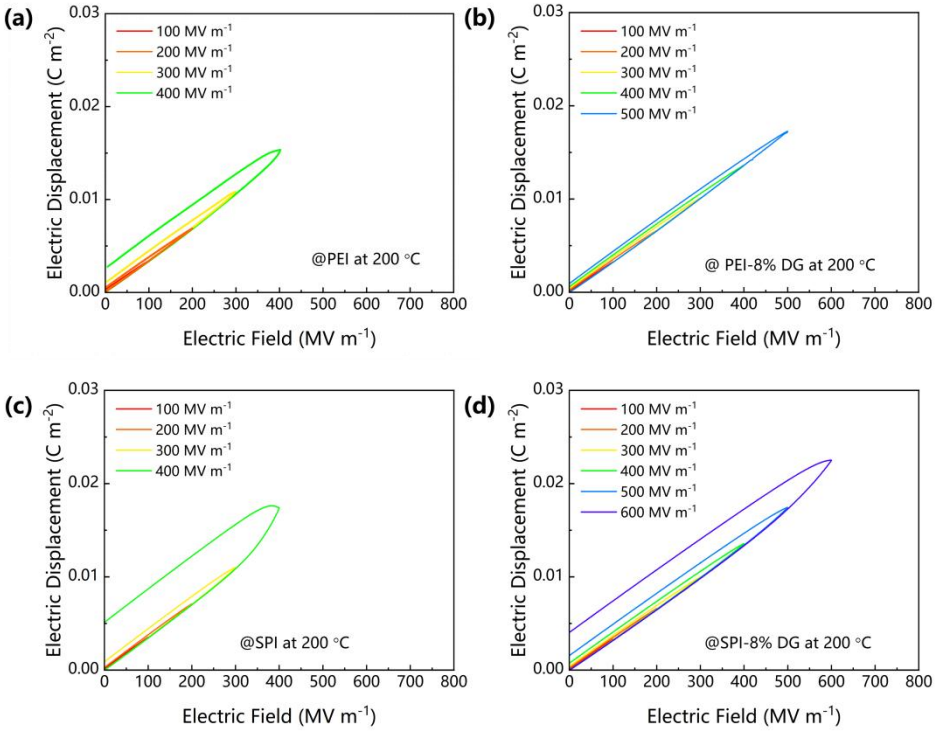

Figure S34. *D*-*E* loops at 200 °C of (a) PEI, (b) PEI-8 wt% DG, (c) SPI, and (d) SPI-8 wt% DG.

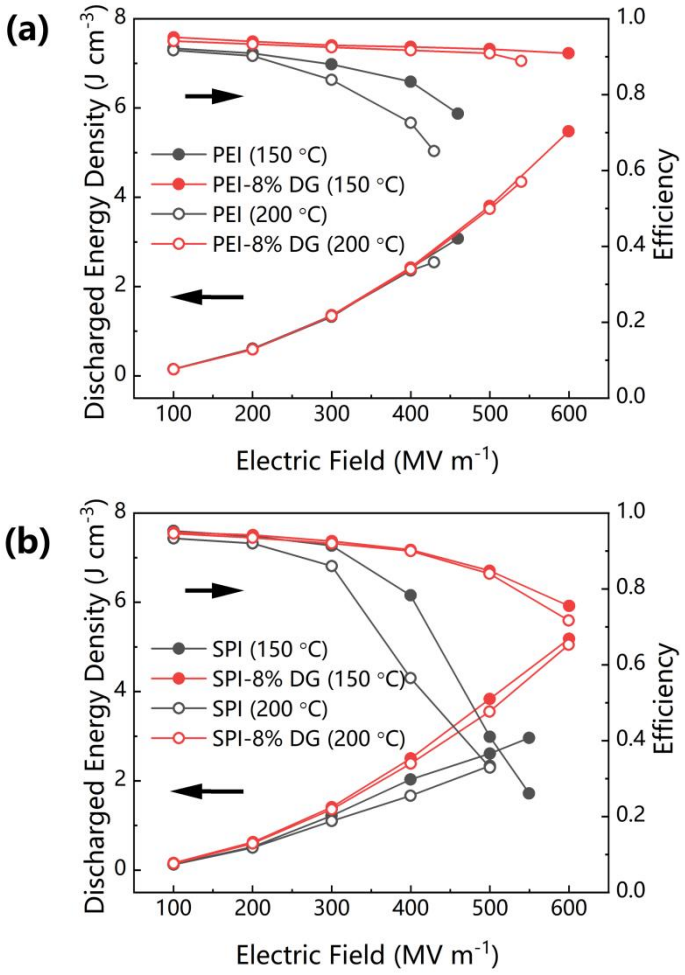

Figure S35. U_d and η versus electric field at high temperatures of (a) PEI-DG and (b) SPI-DG blends.

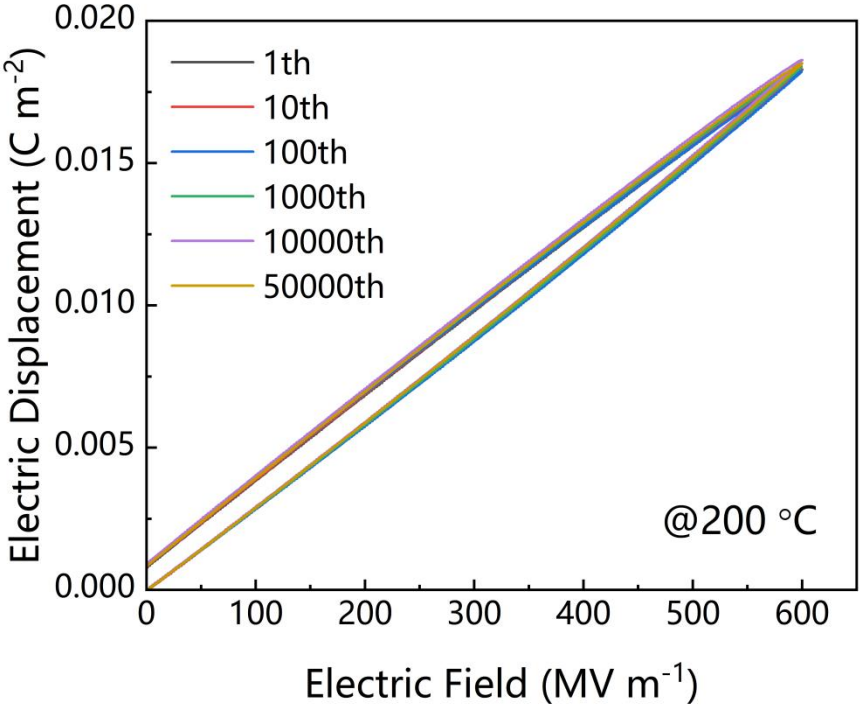

Figure S36. *D-E* loops at different cycles of FPI-8 wt% DG under 600 MV m^{-1} at 200 °C.

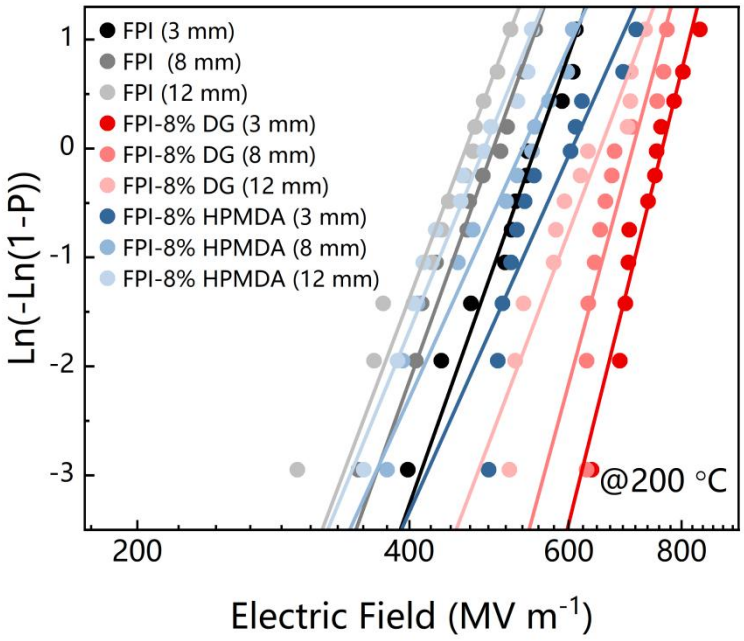

Figure S37. Breakdown electric field Weibull distribution of FPI, FPI-8 wt% DG, and FPI-8 wt% HPMDA with different electrode diameters at 200 °C.

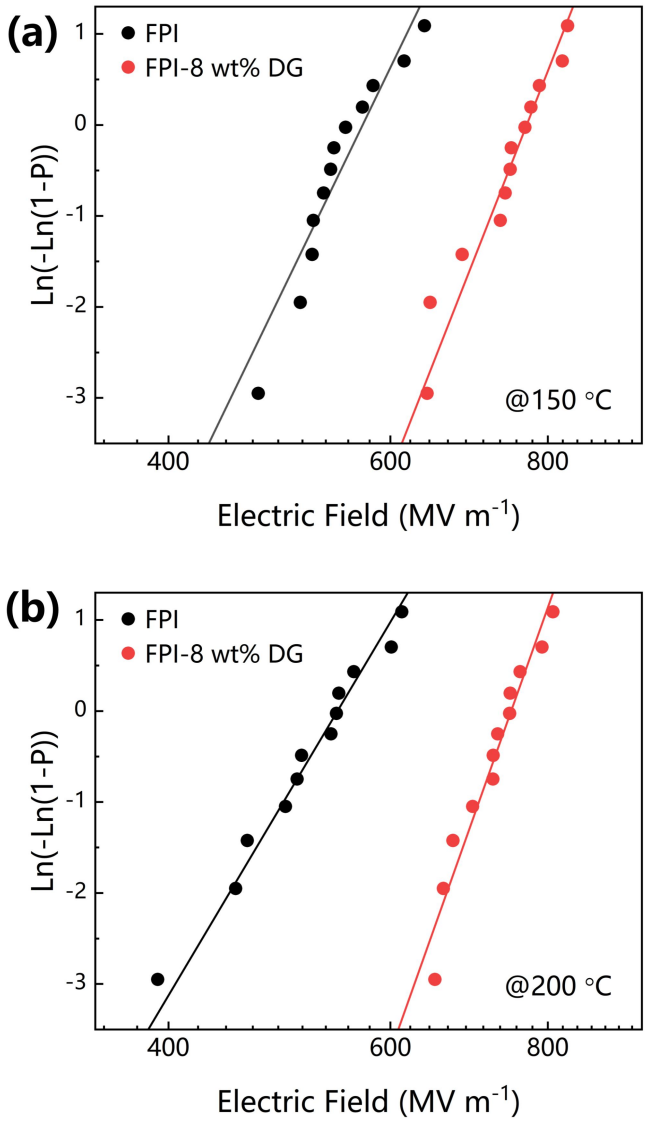

Figure S38. Breakdown electric field Weibull distribution of FPI and FPI-8 wt% DG with aluminum electrodes at (a) 150 °C and (b) 200 °C.

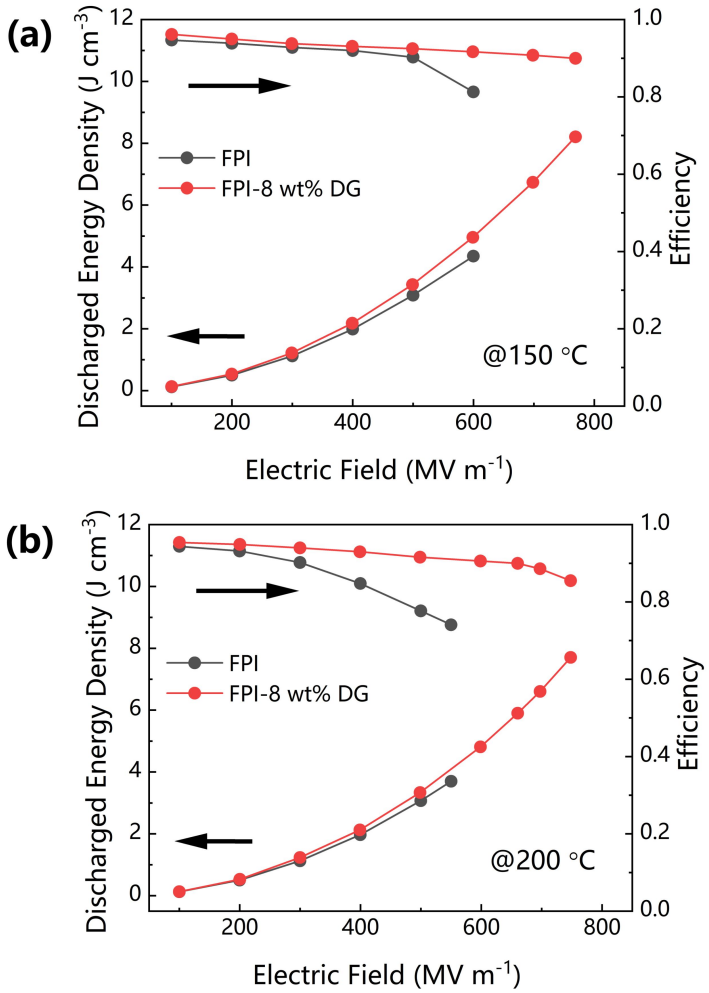

Figure S39. U_d and η versus electric field of FPI and FPI-8 wt% DG with aluminum electrodes at (a) 150 °C and (b) 200 °C.